Rewritable Integrated Photonic Circuits Using Phase Change Materials Actuated by Nanosecond Laser Pulses

Forrest Miller

A thesis

submitted in partial fulfillment of the

requirements for the degree of

Master of Science

University of Washington

2023

Committee:

Arka Majumdar

Mo Li

Program Authorized to Offer Degree:

Electrical and Computer Engineering

University of Washington

Abstract

Rewritable Integrated Photonic Circuits Using Phase Change Materials Actuated by Nanosecond Laser Pulses

Forrest Miller

Chair of the Supervisory Committee:
Arka Majumdar
Department of Electrical and Computer Engineering, Department of Physics

Photonic Integrated Circuits (PICs) are becoming essential for applications such as sensing, communication, and quantum information science. The prototyping process for these circuits, however, requires expensive nanofabrication facilities and irreversible subtractive process steps such as etching. This work demonstrates a platform that implements a prototype passive PIC by using phase change materials actuated by a nanosecond pulsed laser. Using wide bandgap materials Sb_2S_3 and Sb_2Se_3, dielectric assisted waveguides were theoretically shown to guide 1.55 μm light on chip. The calculated losses were as low as 0.0100 dB/um for Sb_2S_3 and 0.0086 dB/um for Sb_2Se_3. An experimental setup using an inexpensive nanosecond pulse laser and a high precision xyz stage was built to experimentally realize this design. Sb_2S_3 films up to 45 nm thick were optically switched. Various patterns were shown to reversibly undergo write, erase, and re-write cycles showing the repeatability and versatility of this setup.

TABLE OF CONTENTS

LIST OF FIGURES

ACKNOWLEDGEMENTS

Thank you to Arka Majumdar for entrusting me with a project containing the perfect balance of theory and experimentation as well as his consistent advice and guidance. Thank you to Sarah Geiger for her suggestions and to The Charles Stark Draper Lab Inc for sponsoring me throughout this project. Thank you to Mo Li for his time and consideration of this work. Thank you to Rui Chen and Johannes Fröch for their assistance and to the whole NOISE lab for their camaraderie and for fostering my burgeoning passion for research.

Chapter 1. INTRODUCTION

1.1 PHOTONIC INTEGRATED CIRCUITS

Photonic Integrated circuits (PICs) allow for the manipulation of light on a chip via devices like Mach-Zehnder Interferometers, ring resonators, directional couplers. Through design this can enable new frontiers in sensors [1], optical communications [2], quantum information science [3], and artificial intelligence [4, 5].

PICs are the optical analog of electric integrated circuits (EICs) such as circuit boards or microchips. The wiring of an EIC guides electricity through the low resistivity metallic wires while the resistive material, FR-4 in circuit boards or silicon dioxide in microchips, serve as insulating regions that do not permit electricity to flow.

This idea is a useful springboard for understanding PICs. Light, as opposed to electricity, is not guided by a difference in conductivity in materials, but rather by a difference in the refractive index of materials. The refractive index is the ratio of the speed of light in a vacuum divided by its speed in a material. Thus, to satisfy conservation of momentum, as the light passes from one material to another, it will change its direction and bend. This phenomenon is familiar to anyone who has placed an object behind a glass of water and observed the distorted image. From the simple ray optics picture, light at sufficiently high angles of incidence will bounce off the material boundary and remain in the material with the higher refractive index. This is called total internal reflection and it describes how light is guided in a photonic circuit (*Figure 1*a). Instead of having higher conductivity, the “wires” in a PIC are made from a material with a higher refractive index. These structures that guide light are called waveguides. A typical infrared integrated waveguide is made by etching silicon to form a ridge. For 1.55 μm light, silicon has a refractive index of 3.5, and air has an index of approximately 1. Therefore, this ridge structure will confine light within the silicon so long as the light hits the silicon/air boundary at an angle greater than

$$\theta_c = \arcsin\left(\frac{n_1}{n_2}\right) = \arcsin\left(\frac{1}{3}\right) \approx 20^o \tag{1}$$

from normal.

One key difference between making light wires and electrical wires is in their dimensional scaling. A circular wire carrying an electrical signal has resistivity that scales as $\frac{1}{r^2}$ where r is the radius of a circular wire. This known scaling law means that electrical circuits can be easily prototyped using millimeter diameter wires and prototyping boards. Waveguides, on the other hand, allow for multiple solutions of Maxwell's equations as their dimensions expand (*Figure 1*c,d). The physical consequence of this is multiple modes of light propagating through the same waveguide. For some applications, such as high throughput data channels, this behavior enables improved performance [6]. For most PICs, however, single mode operation is preferable as the single mode reduces the complexity of the light's interactions. Additionally, single mode operation preserves the amplitude and phase of the light. Therefore, the dimensions of our waveguides must be very precise and small.

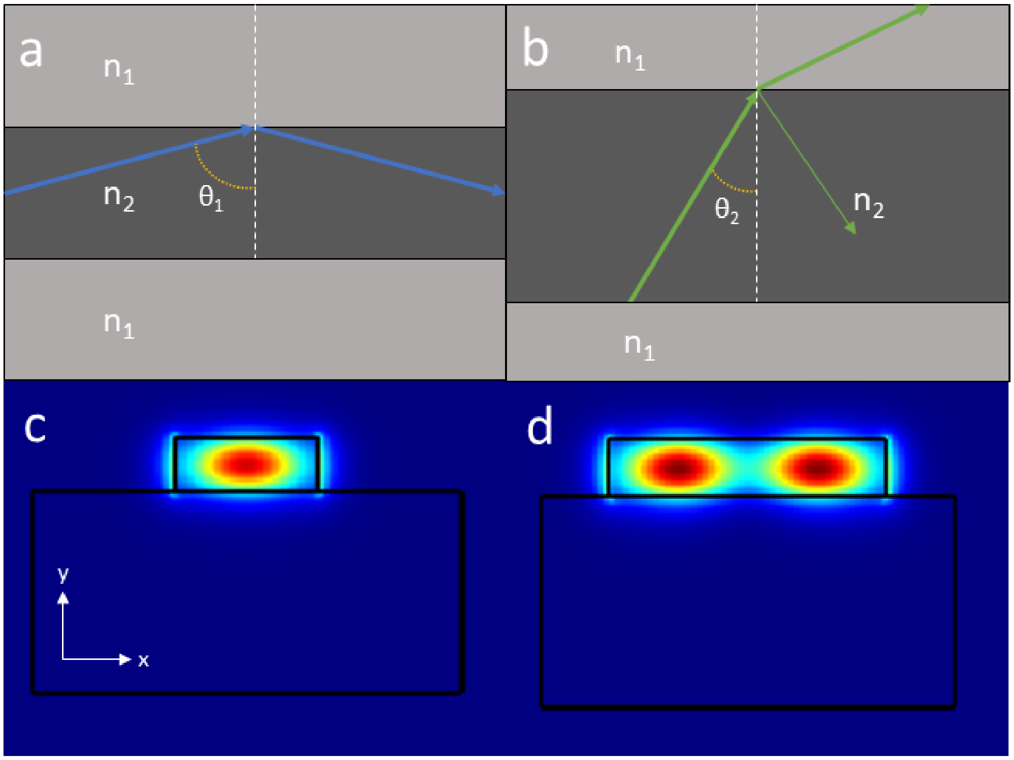

Figure 1: a) A diagram of total internal reflection. Here $n_1 < n_2$ *and* $\theta_c < \theta_1$. θ_c *is defined by equation 1. b) A diagram of a waveguide structure, but where* $\theta_2 < \theta_c$. *Light is not confined in the waveguide in this case. c) A single mode silicon ridge waveguide on a silicon oxide substrate. The ridge measures 500 nm in x and 200 nm in y. d) A multimode silicon ridge waveguide. This structure measures 1.5*μ*min x and 200 nm in y.*

The silicon waveguide discussed above when designed for telecom band light with a 1.55 μm wavelength, has a width of 500 nm. A structure this small is usually made with lithography, a method where a photosensitive material called a resist is applied a silicon wafer then exposed to light shone through a pattern called a mask. The light induces a photo-chemical reaction within the resist which either prevents (in the case of negative photoresist) or allows (for positive photoresist) the exposed regions to be washed away. Once only the patterned photoresist remains on the silicon, an etching solution (potassium hydroxide works well for silicon) eats away at the regions not covered with photoresist. After the etchant is neutralized and photoresist removed, the pattern silicon can guide light. This process almost always takes place in highly controlled environments called nanofabrication facilities. These facilities have the chemicals and specialized equipment to make structures with nanometer precision. These facilities are, unsurprisingly, extremely expensive. For a breakdown of typical costs, see [7], but for now note that a single mask-writing machine can cost more than a million dollars.

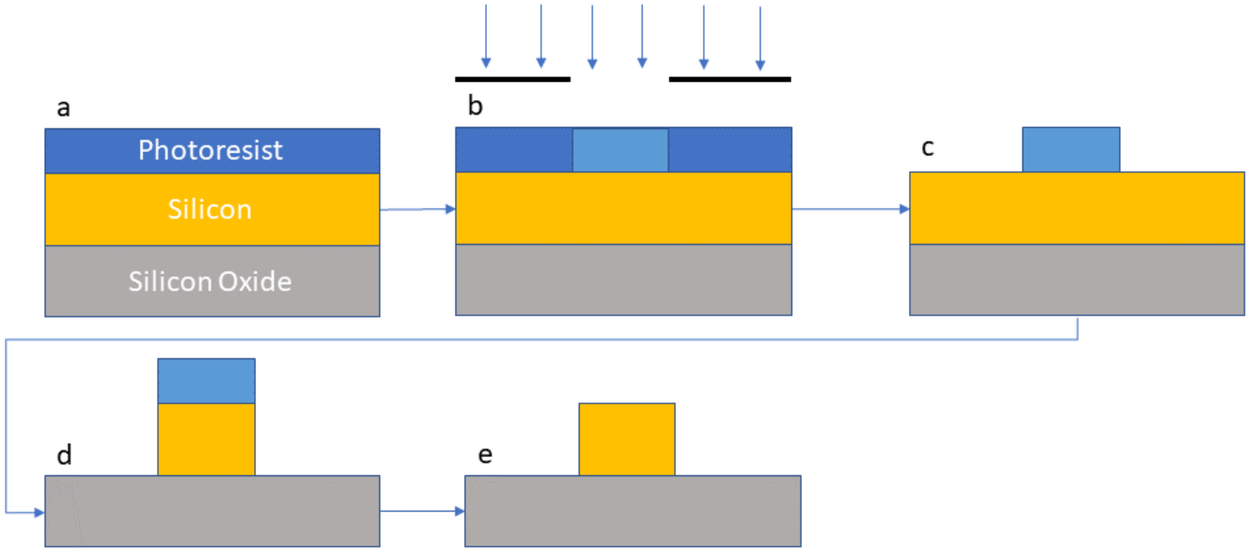

Figure 2: A process flow for making a silicon ridge waveguide starting with a standard silicon on insulator wafer. a) Photoresist is spin coated onto the silicon. b) The photoresist is exposed to light. Here a negative photoresist is used. c) The unexposed photoresist is washed away, and the remaining photoresist is hardened via baking. d) The unprotected silicon is etched away. e) All photoresist is removed.

This lithography process is also used to make microchips such as computer processors. The reason computers are sold for a few hundred dollars is that this process scales very well. Given a mask, a lithography machine can expose a layer of photoresist in a few seconds. Therefore, so long as the design is unchanged enough chips are made such that the marginal cost is low enough for private consumers.

Prototyping, on the other hand, does not benefit from this high throughput manufacturing. A new mask must be made as design is updated. This proves a barrier for PIC research, as researchers without access to a nanofabrication facility must send their design to a foundry. This foundry collects designs from other researchers until enough are ordered to warrant their manufacture. This process takes a long time, typically takes between 4 and 6 months. Researchers with access to nanofabrication facilities, must still spend days in a cleanroom and use tools as they are available. In both cases the manufacturing is costly and time-consuming.

1.2 PHASE CHANGE MATERIALS

A refractive index contrast to guide light on chip can also be achieved by a class of materials called phase change materials [8]. These are materials whose optical properties change dramatically based on the arrangement of their constituent atoms. The two arrangements are either crystalline or amorphous. A PCM in the crystalline state is referred to as cPCM while an amporphous PCM is denoted aPCM. In the crystalline arrangement the atoms form a crystal lattice while in the amorphous state the atoms are assembled in a random orientation. The material can be switched from one state to the other using appropriate heating. The crystalline state is entropically favored, so given enough time at the material’s glass transition temperature, the atoms will arrange themselves in the crystalline state [9]. If the material is heated to its melting point, then the crystal lattice breaks down as the material starts to liquify. If the material is cooled quickly such that the crystalline lattice does not have time to form, then the material is frozen in its amorphous state. Both states are non-volatile due to a large energy barrier that is not exceeded at room temperature. This means no external power is necessary to maintain either the crystalline or amorphous state so long as the material is kept below its glass transition temperature. It is worth noting that this is not a Boolean transition, as partial crystallization or amorphization can occur if the temperature profile does not favor one state heavily enough [10].

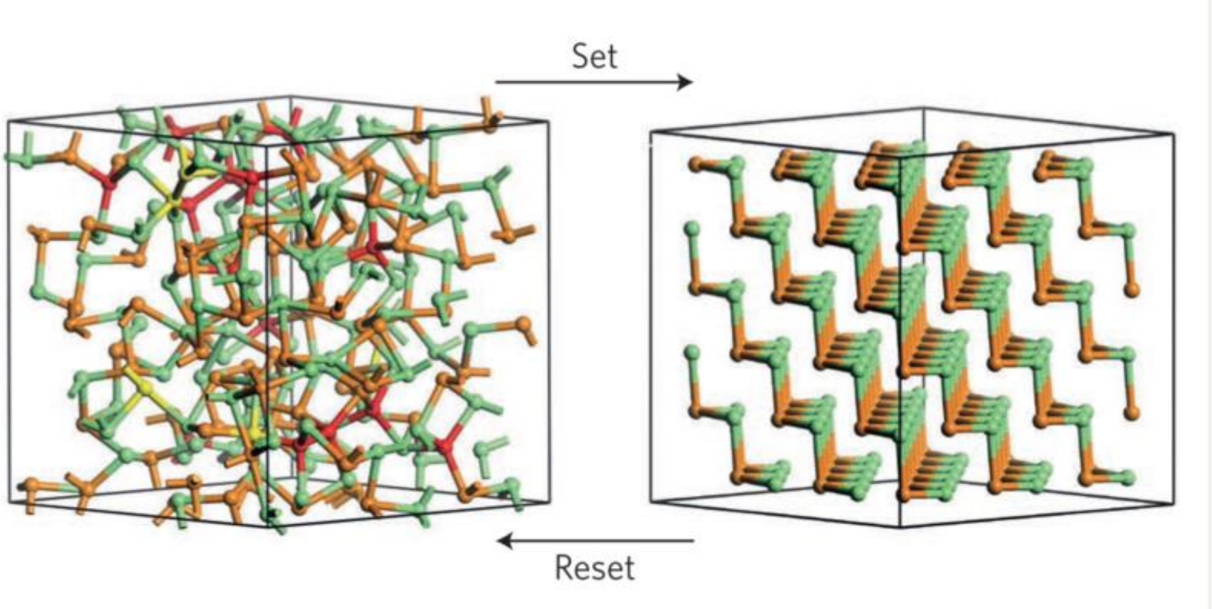

Figure 3: A schematic representation of the amorphous (left) and crystalline (right) states of Germanium telluride, GeTe [11]. The Ge atoms (orange/red/yellow) and the Te atoms (green) are bonded covalently in the amorphous state, but in the crystalline state the three valance electrons are used to form the crystalline sheets. These sheets are resonantly bonded to one another. This difference in bonding leads to a difference in the polarizability of the material, which changes its dielectric function, which in turn changes its refractive index.

1.3 CURRENT USES OF PCMS

Phase change materials were previously used in optical storage devices, most notably compact disks (CDs). The disks are coated in a PCM called $Ge_2Sb_2Te_5$ (GST), which is known for its fast crystallization speed. This allows the material to switch between its amorphous and crystalline states in less than a nanosecond [12]. When information is written on a CD, a high-powered blue laser heats up small areas of the GST. To read the information, a lower powered laser shines on the disk, and the amount of reflected light is measured. Depending on the state of the GST, it is either more or less reflective, thus the reflection is read out as a 1 or a 0. With the improvement of CMOS memory, this use has fallen out of favor, but a lasting consequence were cheap nanosecond pulsed diode lasers used to switch PCMs which will be discussed further in section 3.1.

Currently, PCMs are used as tuning mechanisms on PICs [8]. Due to imperfections during fabrication, some devices have slightly varied behavior that can be corrected using a small patch of PCM. Since the PCM has a non-volatile variable refractive index, it can be adjusted to tune the resonance of ring resonators, change the interference conditions of a Mach-Zehnder interferometer, or alter the path of light in a directional coupler. In this work, instead of using PCMs as a tuning mechanism, the entire device or PIC is made from a blanket film of PCM. Grating couplers can couple light on and off chip (see Section 2.3) forming a rewritable PIC as depicted in *Figure 4*.

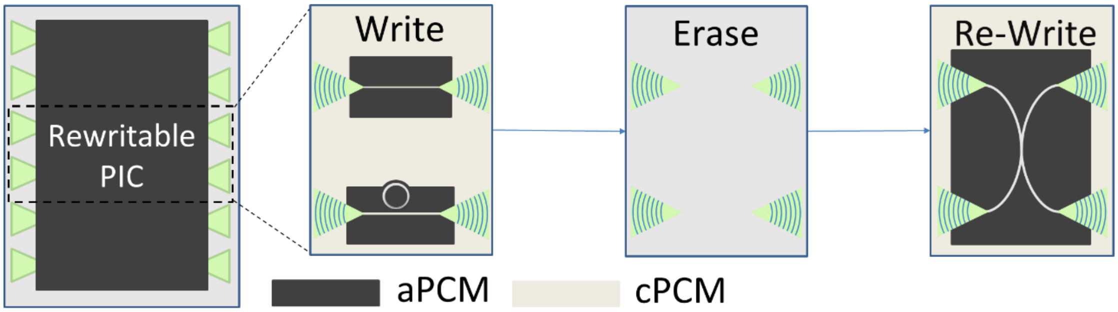

Figure 4: A schematic representation of the re-writable PIC platform in this work. Grating couplers couple light either on or off the PIC and between these grating couplers an arbitrary design can be written. After bulk annealing to crystallize the entire chip, the written patterns are erased, and a new design can be written and tested on the same chip [13].

1.4 LOSSES IN PCMS

The main drawback to PCMs in PICs is they are lossy, i.e., they absorb light as it propagates through the material. This work focuses on PICs that operate in telecom wavelengths around 1.55 µm, so refractive indices will be for these near-infrared (NIR) wavelengths unless stated otherwise. The most well-known PCM, GST, in its crystalline state has an imaginary refractive index $\kappa \approx 1$ in the NIR [14]. When acting as a reflective coating on a CD, this is advantageous, but here the PCM must guide light across a PIC that will span hundreds of microns. Many PCMs have negligible loss in the amorphous state, but even in wide bandgap PCMs Sb_2S_3 and Sb_2Se_3, a non-negligible loss is still present in the crystalline state [15]. This project uses the lower losses of Sb_2S_3 and Sb_2Se_3 as a starting point for the design in Chapter 2. To accurately simulate losses in Sb_2S_3 and Sb_2Se_3, I needed an accurate imaginary refractive index. Ellipsometry values tended to underestimate the PCM loss observed in PICs, so I investigated prior works on PCM-integrated ring resonators. I simulated a waveguide structure in Lumerical’s finite eigenmode solver and adjusted the extinction coefficient of the PCMs until the simulated loss matched the reported experimental results in [10] for Sb_2S_3 and [16, 17] for Sb_2Se_3. From this, I estimated the refractive index in the crystalline state to be $n_{cSbS} = 3.33 + 0.016i$, and $n_{cSbSe} = 4.23 + 0.0043i$. The loss in the amorphous state was negligible for both Sb_2S_3 and Sb_2Se_3 ($n_{aSbS} = 2.76 + 0i$, $n_{aSbSe} = 3.22 + 0i$) and was found from ellipsometry [17, 18]. Given this information about material absorption, I further reduced the loss with the design of the waveguides.

Chapter 2. LOW LOSS WAVEGUIDING DESIGN

2.1 BACKGROUND

Initially, I attempted to confine light in the lower index amorphous material using a distributed Bragg Grating on either side of the waveguide (*Figure 5*). While this required a more complicated structure than a traditional waveguide, it promised near zero propagation loss. The design was predicated on the injected light being unable to leak into the higher index cPCM due to the destructive interference supplied by the Bragg grating. However, in simulation I was unable to get a mode to propagate in the lower index aPCM, so I moved to a traditional waveguide with an added dielectric layer.

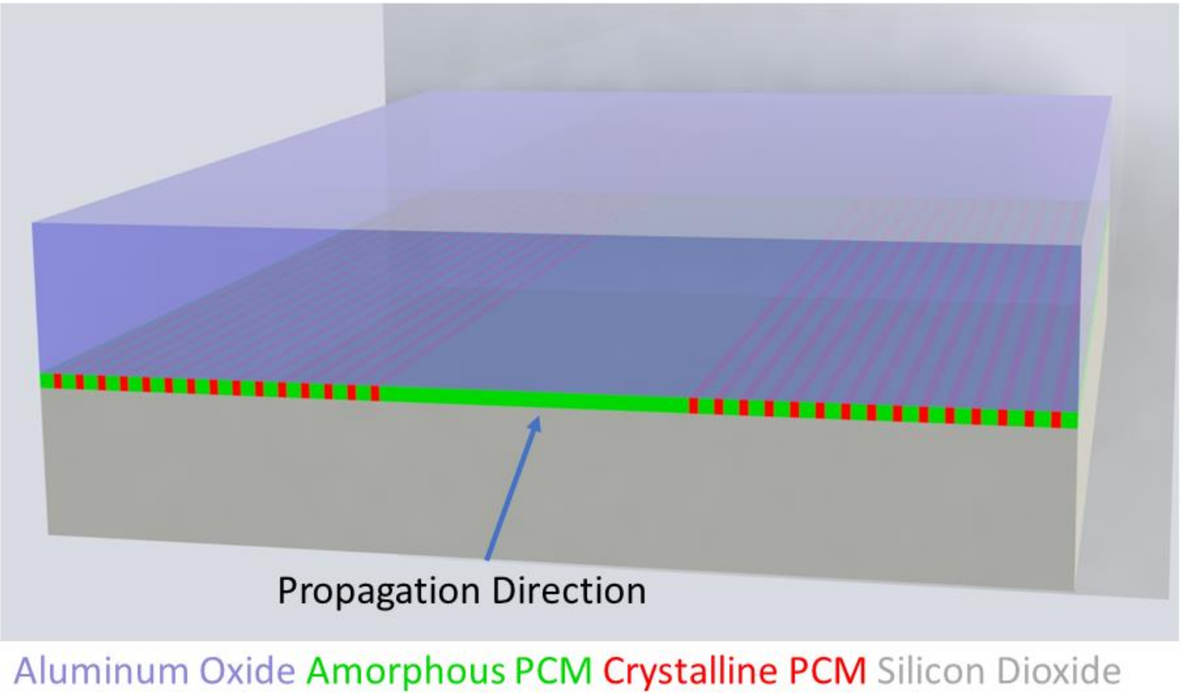

Figure 5: A schematic of the metamaterial distributed Bragg reflector low index waveguide concept. The light bouncing off the amorphous/crystalline layers would destructively interfere with incident light thus preventing its propagation into the crystalline regions.

Now using the higher index crystalline form of the PCM, total internal reflection would guide the mode. If the light were fully confined in a cSb_2S_3 or cSb_2Se_3 core, then the unit propagation loss at $\lambda = 1.55\ \mu m$ is described by $-20\log_{10}\exp\left(-\frac{2\pi}{\lambda} * \kappa_{PCM}\right)$ resulting in a huge unit loss for $cSb_2S_3 \approx 0.56$ and 0.15 dB/μm for cSb_2Se_3. While the loss is overestimated due to the perfect confinement assumption, the result suggests the necessity of a careful waveguide design to achieve a low propagation loss.

One straightforward way to reduce the optical loss is to reduce the PCM thickness, which decreases the interaction between the optical mode and the cPCM. Additionally, thick PCMs are generally harder to fully switch with 70 nm the thickest to date [19]. Moreover, thinner PCM layers enable higher switching endurance [8, 20]. However, an extremely thin PCM layer does not provide enough index contrast to guide a mode. We mitigate this trade-off by exploiting a dielectric-assisted PCM waveguide architecture [21], where a thick dielectric layer of Si_3N_4 [22] is deposited on a thin PCM layer (*Figure 6*). This layer may experience small changes in refractive index during writing, but we anticipate such changes will be negligible [23]. The optical mode is mainly confined in the dielectric layer due to the geometry of the PCM layer, mitigating the absorptive loss of cPCMs. Such a waveguide will be written from the chip's "erased" state, where the PCM layer is uniformly crystalline. A PCM waveguide is created by selectively switching the PCM to the amorphous state. We assume a layer of PCM with a thickness T_{PCM} will be deposited on 2 μm of thermal oxide (SiO_2) film on a silicon wafer. A conformal capping material is needed to prevent material reflow and oxidation during switching [24]. Therefore, we encapsulate the PCM with 20 nm of atomic layer deposited Al_2O_3 and then deposit a Si_3N_4 layer with thickness T_{clad} to create the material stack (*Figure 6*).

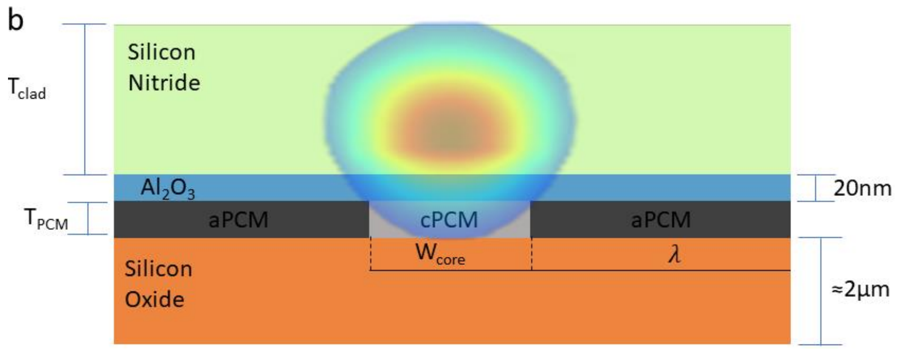

Figure 6: Schematic of the low-loss dielectric assisted waveguide. A thin PCM layer provides the index contrast to guide the mode and a thick dielectric layer contains most of the mode [13]. This significantly reduces the loss by reducing the interaction between the cPCM and the light.

2.2 LOW LOSS WAVEGUIDE SIMULATION

We optimize the waveguide geometry for low loss, using the Finite Element Eigenmode (FEM) solver in Ansys Lumerical. We start by sweeping the Sb_2S_3 thickness T_{PCM}, and the cSb_2S_3 core width W_{core}. Unsurprisingly, a thinner T_{PCM} yields a lower loss. However, below a thickness of 12 nm, the PCM cannot confine a mode. The simulation values for $T_{PCM} < 12$ nm are numerical artifacts that arise from the finite dimensions of the simulation region. Since the PCM must guide the mode while introducing minimal loss, a layer thickness of 15 nm and a core width of 2.0 µm is used. The thickness of the Si_3N_4 layer is set at 0.4 µm as shown in *Figure 7*b. This is the thickest Si_3N_4 layer that supports single mode operation. This structure exhibits a propagation loss of 0.0100 dB/µm.

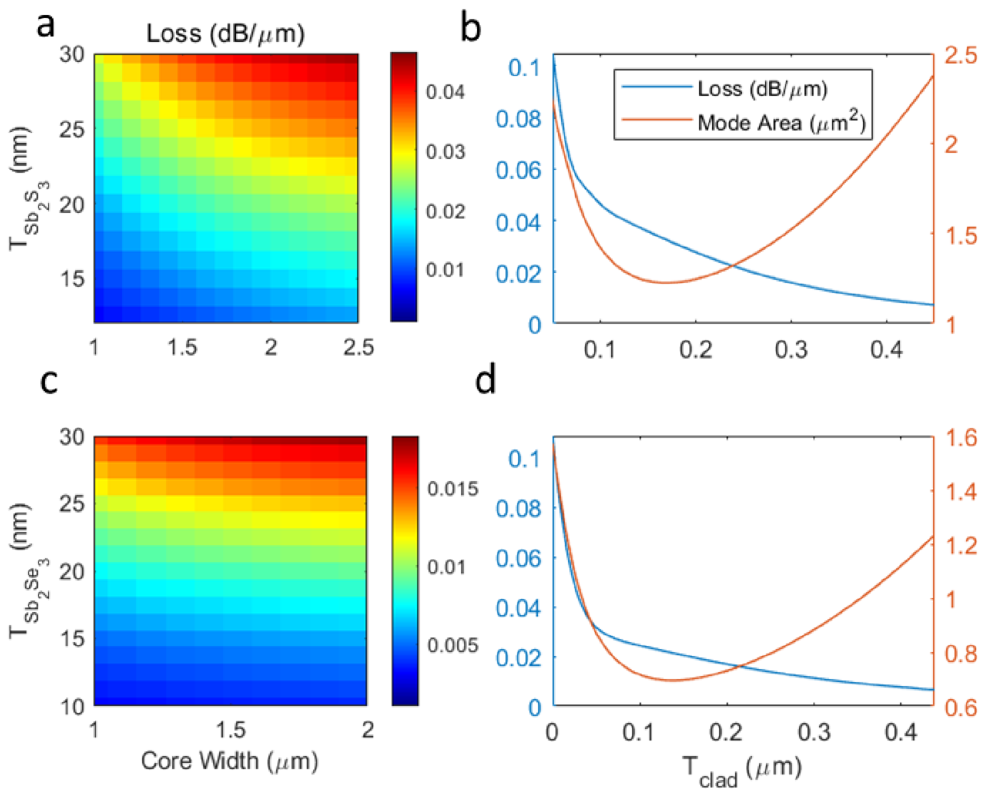

Figure 7: a) Waveguide loss in dB/μm for a joint parameter sweep of the Sb_2S_3 thickness and waveguide core (cSb_2S_3) width. b) The loss and effective mode area as a function of the Si_3N_4 thickness in the Sb_2S_3 design. c) Waveguide loss (dB/μm) for a joint parameter sweep of the Sb_2Se_3 thickness and waveguide core (cSb_2Se_3) width. d) The loss and effective mode area as a function of the Si_3N_4 thickness in the Sb_2Se_3 design [13].

The loss in the Sb_2Se_3 waveguide exhibits much weaker dependence on W_{core}. This is due to the higher real refractive index of Sb_2Se_3, which gives tighter mode confinement. We choose 1.5 μm as the core width to improve integration density. Similar to the Sb_2S_3 design, the loss increases with increasing T_{PCM}. Here we choose 20 nm as the layer thickness. This T_{PCM} is thin enough to switch and provide low loss while reliably guiding a mode. The Si_3N_4 thickness was set to 400 nm to minimize loss while confining a single mode. This geometry demonstrates a loss of 0.0086 dB/μm.

We note that while a Sb_2S_3 thickness of 15 nm is sufficient for a straight waveguide, a bent waveguide requires slightly thicker PCM and/ or thinner Si_3N_4 to more tightly confine the mode. Based on simulation, a T_{PCM} of 25 nm PCM and a 100nm T_{clad} will be guide light across a 75 µm (25 µm) bend using Sb_2S_3 (Sb_2Se_3). These new parameters increase the loss by a factor of 8 (4), but support bending, which is critical for any integrated photonic device. With this architecture, we believe we can optically write directional couplers, Y-splitters and ring/ disk resonators [25]. Components like mode-converters or waveguide crossings rely on small features, and our rewritable PIC may not be suitable to write such small features.

2.3 ON/OFF CHIP COUPLING

The PICs presented here must interface with free-space optics to input and read out the optical signal. We propose to accomplish this using fixed grating couplers on the chip, forming optical input/output ports, between which designs can be written, erased, and re-written (*Figure 4*). Edge coupling would also work with this design, but we envision grating couplers enabling easier interfacing. These grating couplers are formed by etching the Si_3N_4 layer since the optical modes for both designs are primarily confined in the Si_3N_4 layer (*Figure 6*). While this etching step is exactly what we intend to eliminate, we note that after this one etch, thousands of PIC designs can be written and tested on this platform without further etching [15]. It is possible to write grating couplers into the PCM, but such couplers suffer from low coupling efficiencies and must be re-written after each anneal. We optimize these gratings for maximum coupling efficiency using single mode fibers at 25 degrees of incidence using Lumerical's Finite Difference Time Domain (FDTD) simulation. In the Sb_2S_3 design, a grating pitch of 1.01 µm, a duty cycle of 0.8, and an etch depth of 180 nm resulted in a coupling efficiency of 21%. In the Sb_2Se_3 design, a grating pitch of 0.97 µm, a duty cycle of 0.56, and an etch depth of 240 nm also resulted in a coupling efficiency of 21%. The gratings are connected to the waveguides via a tapered section with end width of 4 µm for both PCMs, which yields a mode overlap of more than 95% with the guided modes.

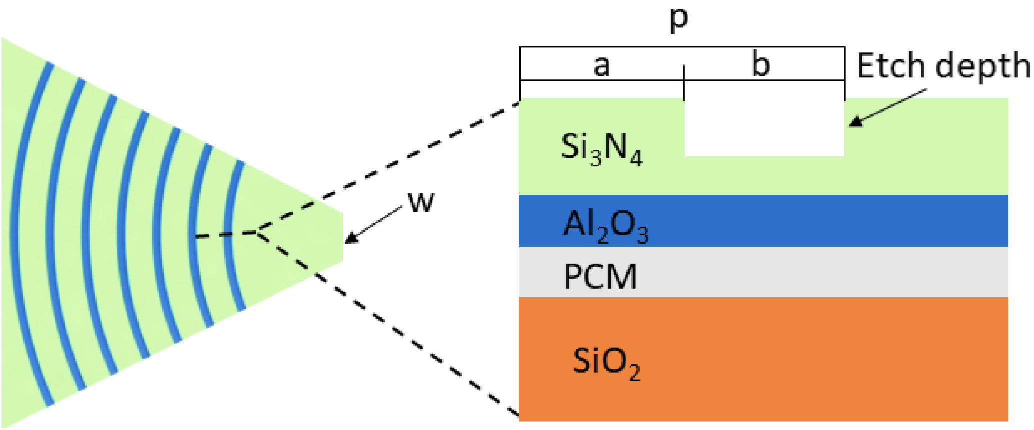

Figure 8: Grating coupler and the two-dimensional cross-sectional view along the dashed line. P, the optimal pitch, is 1.01 (0.97) µm for the Sb_2S_3 *(*Sb_2Se_3*) design. The optimal duty cycle, a/b, is 0.8 (0.56) for the* Sb_2S_3 *(*Sb_2Se_3*) design. The etch depth was 180 (240) nm for* Sb_2S_3 *(*Sb_2Se_3*). In both cases, a taper end width, w, of 4 µm provides > 95% mode overlap between the coupler and the waveguide.*

2.4 SIMULATED NANOSECOND SWITCHING

The PICs can be switched using a pulsed laser as the absorbed light is dissipated as heat which actuates the phase transition. The arbitrary patterning can be accomplished by a programmed three-axis translation stage. I simulated four pulse schemes with different spatio-temporal pulse shapes (*Figure* 9a-d) in COMSOL Multiphysics and selected the pulse that best amorphizes the PCM. I only consider amorphization here as the sample will start in the erased state which is uniformly crystalline. To return to the erased state, the chip will be bulk annealed on a hot plate, excluding the laser from the crystallization process. I expected the ideal laser pulse shape to be a rectangular spatial shape to provide a smooth boundary region and an increasing temporal shape to produce uniformly switching in the depth direction.

However, I found that a Gaussian spatial shape and rectangular temporal shape can switch thin Sb_2S_3, offering a simple experimental realization. 450 nm wavelength pulses were delivered directly to the 15 nm film of Sb_2S_3 (n = 4.12 + 1.80i) in *Figure 6*, so reflection off the alumina and Si_3N_4 layers is not considered. The pulses had either a Gaussian or uniform spatial distribution and either a rectangular or exponentially decaying temporal distribution. All pulses last approximately 14 ns and the power values were adjusted to achieve a maximum temperature of approximately 900 ^{o}C.

A successful amorphization pulse must satisfy four conditions. First, enough thermal energy must be applied to completely melt the PCM. This requires the delivered energy to heat PCM to its melting temperature and further overcome the latent heat, given by the multiplication of enthalpy of fusion (ΔHf) and mass of the PCM. Second, the cooling rate must exceed $\sim 1\ K * ns^{-1}$ [11]. This ensures the PCM is frozen in the amorphous state [9] and does not undergo unintentional recrystallization. Third, the absorbed thermal energy must not heat the PCM above its boiling point T_b, which irreversibly ablates the material. We obtain Sb_2S_3 parameters from the literature for the simulations: the melting point is T_{mp} = 547 ^{o}C [15], the enthalpy of fusion is ΔHf = 47.9 $\frac{kJ}{mol}$, the boiling point is T_b = 1149 ^{o}C, the density is 4.56 $\frac{g}{cm^3}$, the specific heat is 575.4 $\frac{J}{kg*K}$, and the thermal conductivity is 0.42 $\frac{W}{m*K}$ [10, 26]. Lastly, the boundary region between switched and non-switched regions defines the waveguide edge. This boundary contains material heated to its melting point but not enough to exceed its enthalpy of fusion. This implies a partial amorphization, where a portion of the crystalline structure remains. This is undesirable as a more abrupt index change at the boundary could lead to better mode confinement.

I examined different pulse conditions against these criteria. As shown in *Figure 9*a-d, all pulse conditions exceed the melting point and achieve a faster cooling rate than $1\ K * ns^{-1}$. Our hypothesis for temporal modulation was that an exponential ramp would more uniformly heat the Sb_2S_3 layer along its thickness in the vertical direction. This statement is supported by the more linear average temperature curve in *Figure 9*c,d. However, since the Sb_2S_3 layer is very thin, there was little variation in temperature from the top to the bottom of the Sb_2S_3 film. Therefore, we can consider pulses with rectangular temporal modulation. In a thicker PCM layer, we anticipate that temporal modulation of the beam power could enable more uniform heating in the depth direction.

The performance difference between the spatial beam shapes is apparent in the feature size and the boundary region width. A Gaussian mode is better if the desired circuit requires fine features. This is a direct result of the narrower intensity distribution of a Gaussian compared to a uniform beam. With a Gaussian beam, the width of the switched PCM could be smaller than the laser's spot size if the laser power is tuned such that the beam's full-width-half-maximum is lower than the amorphization threshold. A uniform beam lacks this ability to achieve a small feature size. However, its advantage is a narrower boundary region in the Sb_2S_3. The boundary region for the Gaussian beams traverses a distance of 105 pm (*Figure 9*e). In comparison, the boundary is only 27 pm (*Figure 9*f) for a spatially uniform beam. This shorter boundary resembles the step-index profiles used in our previous simulations and leads to better mode confinement. Our thermal simulation verifies that the thin Sb_2S_3 layer can be switched entirely with nanosecond laser pulses and offers a simple experimental realization with a natural laser beam with a Gaussian spatial and rectangular temporal shape. Sb_2Se_3 has a thermal conductivity 0.76 times that of Sb_2S_3 and a volumetric heat capacity 1.7 times that of Sb_2S_3 [10]. These similar thermal parameters suggest nanosecond laser switching of Sb_2Se_3 is possible as well.

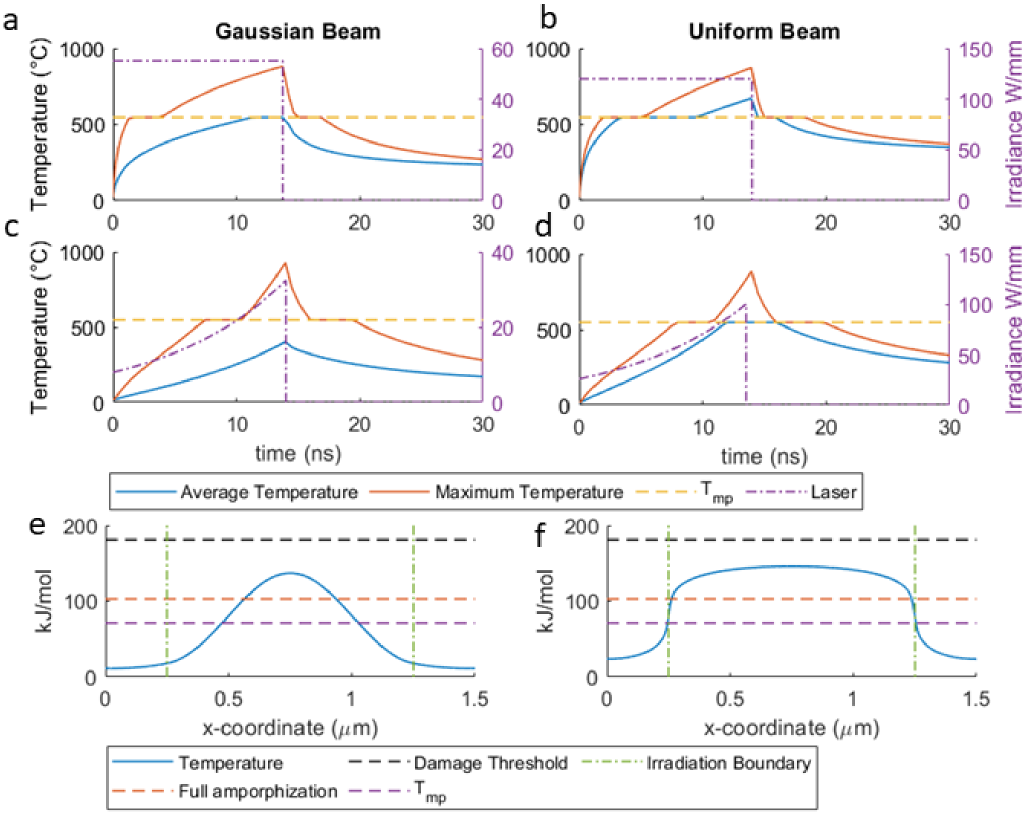

Figure 9: a-d) The transient thermal dynamics for different pulses: a) temporally rectangular, spatially Gaussian, b) temporally rectangular, spatially uniform, c) temporally exponentially decaying, spatially Gaussian, d) temporally exponentially decaying, spatially uniform. e, f) Static temperature profile along the spatio-temporal line cut at y = $T_{SbS/2}$ *and t = 14 ns for e) a spatially Gaussian beam and f) a spatially uniform beam. The Gaussian beam switches a smaller area of* Sb_2S_3 *than the uniform beam, but the uniform beam has a shorter boundary region (the distance between* T_{mp} *and full amorphization). Thus, a Gaussian beam can write finer features, but a uniform beam will likely have better mode confinement [13].*

2.5 CONCLUSION

In this section, the concept of PICs and PCMs were introduced, along with the issue of optical loss in a PCM waveguide. This loss was mitigated by a dielectric assisted waveguide structure which reduced the loss by a factor of 56 for Sb_2S_3 and 17 for Sb_2Se_3 over a traditional waveguide. I found parameters for grating couplers that act as the in/out ports of the PIC, then demonstrated that a nanosecond laser in this material stack provides a fast enough cooling rate to switch the PCM from its crystalline to the amorphous state. These theoretical results will be tested experimentally in the following chapter.

Chapter 3. EXPERIMENTAL SWITCHING

3.1 BACKGROUND

Using PCMs to make integrated photonic devices such as metasurfaces, ring resonators, directional couplers, and Mach-Zehnder interferometers have been demonstrated previously [10, 27]. In most of these works, the PCM switching used a femtosecond laser pulse or electrical switching. The extremely fast irradiation from a femtosecond optical pulse guarantees the cooling rate will be fast enough to amorphize the PCM. These lasers, however, typically cost hundreds of thousands of dollars due to the wide gain spectrum and mode locking that generates such short pulses. Nanosecond lasers, on the other hand, are slow enough to be turned on and off electrically. This reduces the price significantly. Further price reductions came from the popularity of Compact Disk (CD) storage which incentivized inexpensive production of nanosecond pulsed lasers to change the phase change material GST on the disk’s surface. The ThorLabs NPL45C laser used in this work costs less than two thousand dollars. Electrical switching is advantageous because it is integrated on chip and does not need an external setup aside from a voltage source. However, the electrical contact pads and doped silicon heaters become fixed features on chip and therefore do not meet the flexibility of arbitrary designs in this work. That restriction does limit this setup to testing passive PICs, but testing PICs without modulation or other active features will still be a useful step in the design/ prototyping cycle. One work demonstrates switching GST with nanosecond pulses, but as mentioned previously, the loss in this material makes it unsuitable for PICs [28].

The operative question in this section is if the longer nanosecond duration pulse will match with the theoretical results in section 2.4, or if the longer exposure will not result in reliable amorphization.

3.2 Setup

To switch thin films of Sb_2S_3 we used a Thorlabs NPL45C laser coupled to a 0.1 µm core diameter multimode fiber to supply a quasi-single mode beam to a 100x magnification and 0.9 numerical aperture (NA) objective which focused the light onto the sample. The fiber coupling was necessary to correct the beam spot as the intensity profile from the semiconductor laser was highly elliptical. It was originally corrected with an anamorphic prism pair, but after the laser power was found to be much higher than needed, the fiber was used to achieve the final mode profile. Ideally, a single mode fiber would have been used, but the smaller core diameter of a single mode fiber did not capture enough light to switch the Sb_2S_3. The free space coupling efficiency was 4.4% with the multi-mode fiber.

This laser light was then reflected to the sample through the objective. The sample was illuminated with a white LED and imaged with a ThorLabs DCC1545M camera. See *Figure 10* for a depiction of the setup.

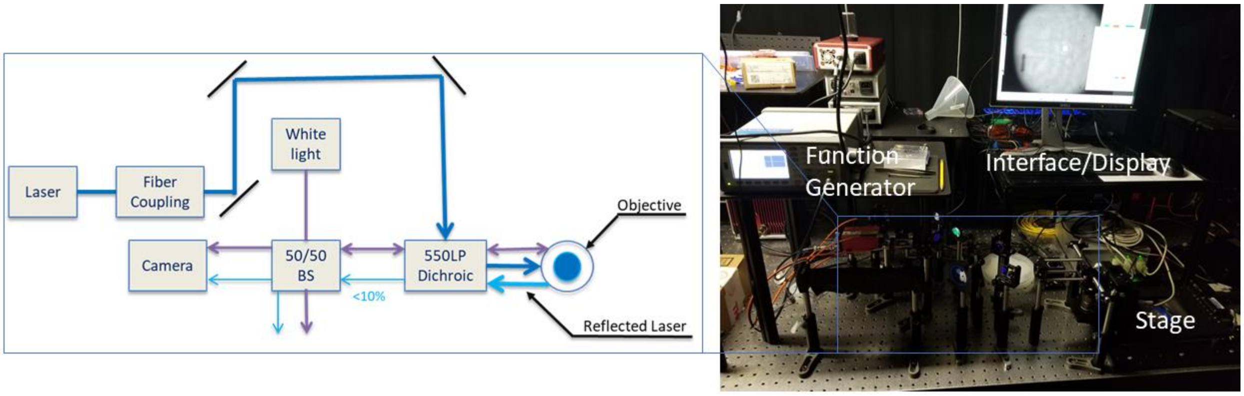

Figure 10: (left) A schematic of the laser writing setup. (right) A picture of the experimental setup for this work.

The largest challenge in making this setup was maintaining the laser's focus as the stage travelled. The stage itself (a Mad City Labs microstage) was capable of 100 nm incremental movement over a 25 mm travel distance. This resolution is high enough that the laser spot size limits the resolution of the setup, but to achieve the small spot size, a high NA objective was used. This limits the depth of focus, given by

$$d < \frac{\lambda}{NA^2} = \frac{450nm}{0.9^2} = 555\ nm \tag{2}$$

As the pattern is written, the sample must remain within half a micron of the vertical datum. While the sample stage is as flat as practical, only patterns less than 50 µm could be drawn reliably without a dynamically varying focus. To address this, I wrote a program that took three pre-measured points on the chip and defined a focal plane from these points. As the stage progressed through a pattern, the program dynamically assesses the x and y coordinates and adjusts the z position to remain on that plane. This enabled reliable writing of patterns more than 250 µm in diameter.

The written PICs were measured on a separate setup where a 1.55 µm fiber coupled laser was directed to a grating coupler and a fiber coupled optical power meter collected light from the other grating coupler in the PIC.

3.3 WRITING RESOLUTION

The maximum resolution of the writing laser is dictated by the diffraction limit given by equation 2.

$$d = \frac{\lambda}{NA} = \frac{450nm}{0.9} = 250nm \tag{2}$$

Where d is the diameter of the full width half maximum of the optical intensity, lambda is the wavelength of light, and NA is the numerical aperture of the objective lens. For this setup, the wavelength of the writing laser is 450 nm and the numerical aperture of the objective is 0.9, so the diffraction limited spot size is 250nm.

The resolution of the writing laser does not completely dictate the pattern resolution as the pattern is formed by the switched PCM. Specifically, if the laser power is very high, the thermal gradient would melt material outside of the laser spot. Conversely, if the laser power is tuned such that the half maximum of the laser power does not melt the PCM, then the switched region will be smaller than the full width half maximum of the laser spot. The resolution of this setup is shown in *Figure 11*.

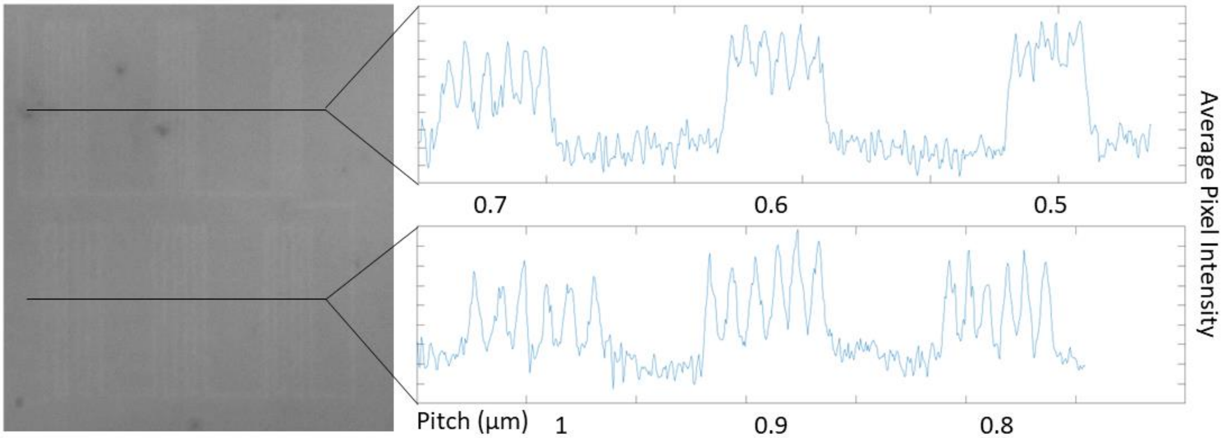

Figure 11: (left) Optical microscope image of laser switched lines of Sb_2S_3. The lighter colored lines are laser written a Sb_2S_3 while the darker background is cSb_2S_3. The pitch of the lines decreases from left to right. (right) Plots of greyscale pixel magnitude across the black lines. The pixel values in the vertical direction were averaged to form each value in the horizontal direction.

From Figure 11, the setup is capable of writing patterns with a line pitch greater than 0.6 µm, close to the diffraction limit ~0.5 µm pitch. From the full width half maximum of the peaks in Figure 11, the spot size is measured around 280 nm which is near, but not at the diffraction limit. It is worth noting that this distance corresponds to 8 pixels in the CCD camera. Thus, this measurement has a special resolution of 35 nm. The roughness is *Figure 11* (left) is largely due to this limited resolution. This experiment also used discrete neutral density filters in 0.1 dB increments. This result could likely be improved using a continuous ND filter to more accurately tune the laser power.

3.4 PULSE CONDITIONS

Using the material stack proposed for Sb_2S_3 from section 2.2, I found a range of pulse conditions that reversibly switch a 15 nm Sb_2S_3 film from the crystalline to the amorphous state as shown in *Figure 12*a. Since fluence is the key metric in switching, note that a 73 mW peak power corresponds to a fluence of 1.19 W/um. To switch from the amorphous to the crystalline state, the sample was bulk annealed on a hotplate a 325 ^{o}C for 12 minutes.

I verified the successful switching of the samples by Raman spectroscopy. The crystalline lattice of cSb_2S_3 demonstrates specific vibrational modes that can be excited by an incident photon. The inelastic collision of these photons is measured by the Raman spectrometer, and the expected vibrational modes at 125, 154, 188, 240, 284, and 312 cm^{-1} (*Figure 12*d). If the material is in the amorphous state, then these vibrational modes do not exist, and the spectrum would be a smooth curve as shown in *Figure 12*c.

The experiment to find switching parameters consisted of writing a grid of 50 μm squares. In each column, the pulse power was adjusted by placing a different ND filter before the dichroic mirror. The pulse duration varied in each row was adjusted manually on the laser. An optical image of this experiment and associated results are shown in *Figure 12*.

In this experiment, the stage wrote each square from left to right while traveling at a speed of 0.02 mm/s. The laser's repetition rate was set to 2 kHz.

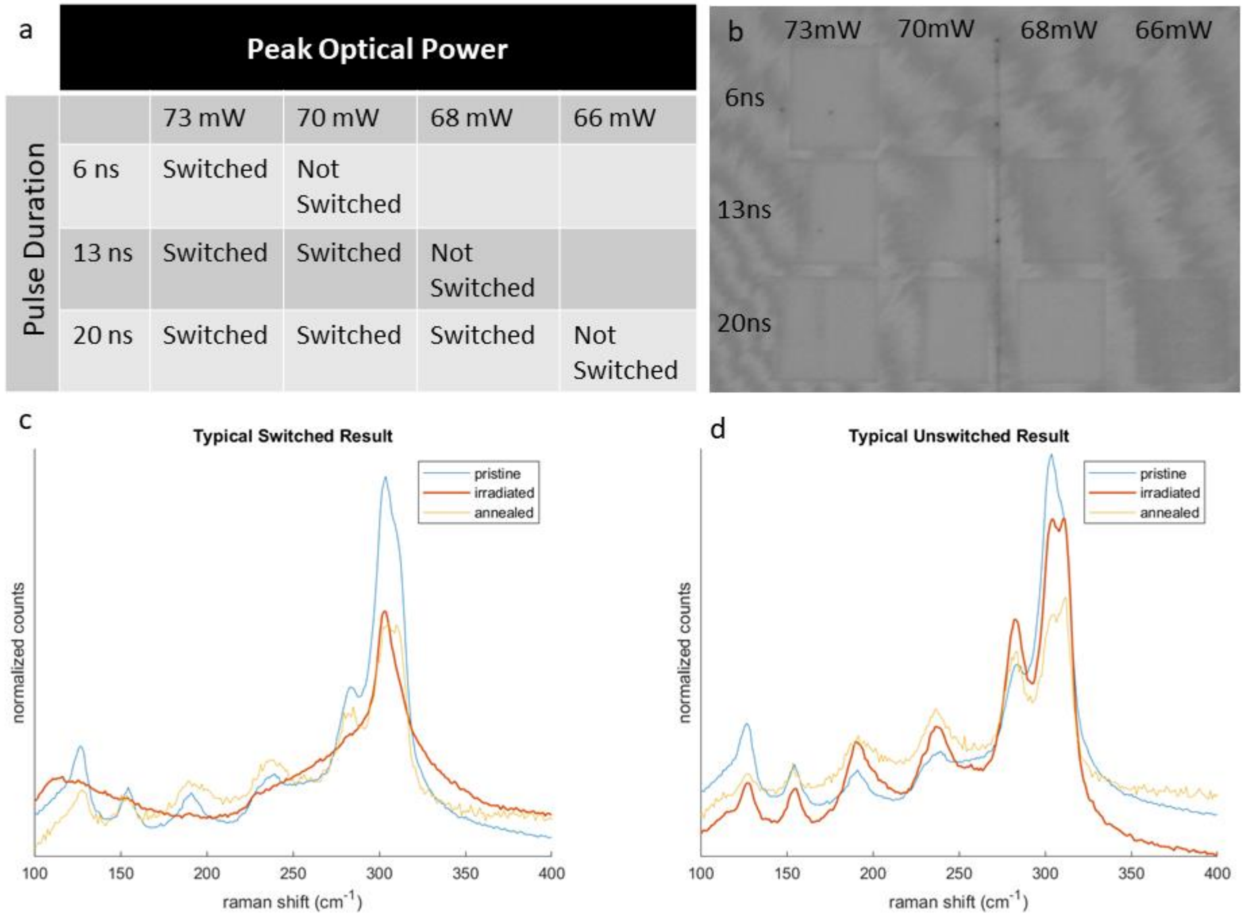

	Peak Optical Power			
Pulse Duration	73 mW	70 mW	68 mW	66 mW
6 ns	Switched	Not Switched		
13 ns	Switched	Switched	Not Switched	
20 ns	Switched	Switched	Switched	Not Switched

Figure 12: a) A table showing switching events as a function of peak optical power and pulse duration. b) An optical image of the switched regions. c) A typical Raman spectrum for a switched result. d) A typical Raman spectrum for an unswitched result.

The lower triangular region of the pulse duration/ peak optical power matrix all switched from the crystalline state to the amorphous state, achieving Raman spectra similar to *Figure 12*c. This follows the intuitive trend that lower pulse powers can still achieve the heating necessary to switch the Sb_2S_3 layer, given the material is exposed for a longer pulse duration. This trend should continue until the cooling rate once the laser is turned off becomes too slow to facilitate reliable amorphization, or when the laser power is high enough to cause material ablation. Sb_2S_3 layers up to 45 nm were switched without altering the pulse conditions in *Figure 13*. Upper bounds for laser power were not explored as they may damage the material and would have unreliable resolution.

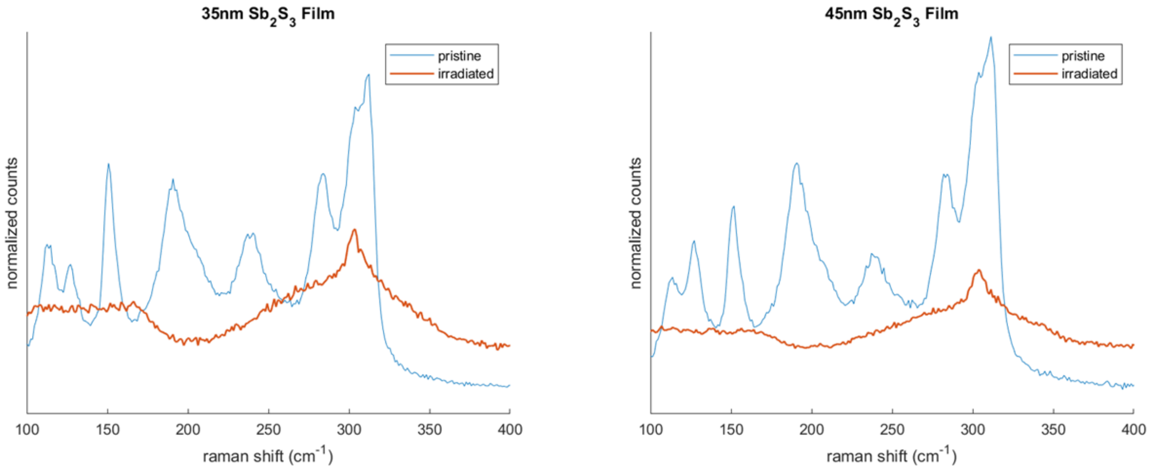

Figure 13: Raman spectra for 35 nm (left) and 45 nm (right) Sb_2S_3 films before and after irradiation.

3.5 REVERSIBLE WRITING

Patterns for this setup take the form of rows of (x,y) coordinates. The stage will read one set of coordinates, subtract each x and y value from its current position, then move a distance equal to the difference in the respective axis. These tables of coordinates were created either manually in

MATLAB or by a script I wrote to reduce the GCODE file from a 3d slicer program into a coordinate table. One pattern from each method is shown in *Figure 14*.

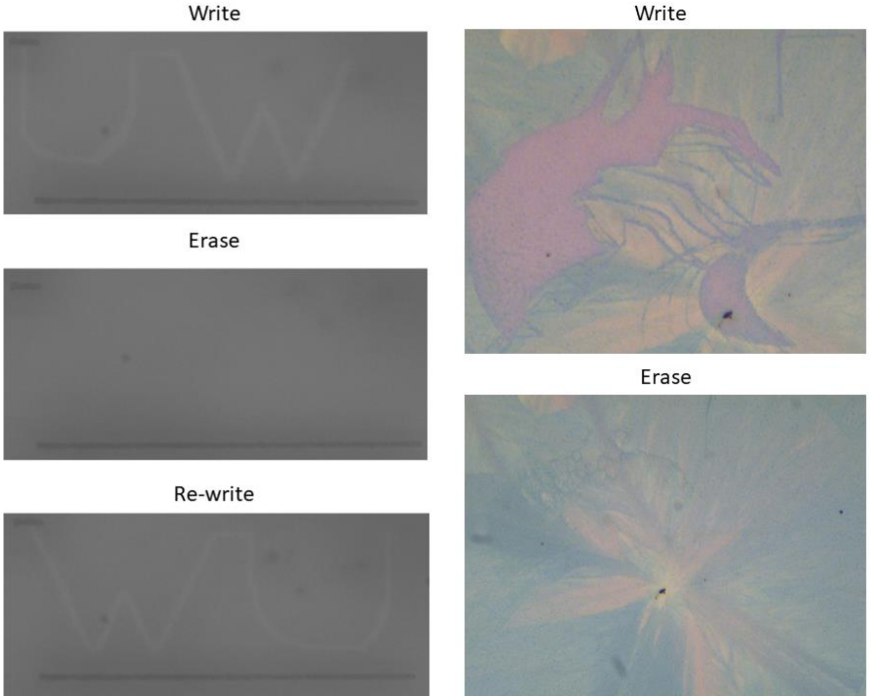

Figure 14: (left) An optical image of the letters "UW" written in aSb_2S_3 *on a c*Sb_2S_3 *background. Annealing erased the pattern at which point "WU" was written on the same area. (right) A bitmapped image of a husky was fed through the 3D slicer program and then its coordinate file was executed to draw the husky on chip. The pattern was then erased.*

Here we demonstrate two cycles of rewritability, but Sb_2S_3 can by cycled at least 2000 times [15]. An unexpected benefit of Sb_2S_3 was its slow crystallization speed. This implies that upon laser heating, the amorphous state is heavily favored. In experiment, this meant the same region of Sb_2S_3 could be exposed to the laser without risking crystallization. In experiments with GST, the pulse repetition rate had to be matched to the sample stage's travel speed because if the same region were exposed multiple times, it would cause either partial or full re-crystallize during the amorphization step. In Sb_2S_3, however, the repetition rate of the laser pulse is irrelevant between

100 Hz and 10 MHz. This allows patterns to be corrected after they are written. If part of a pattern fails to switch, it can be easily filled in by running a subsection of the program.

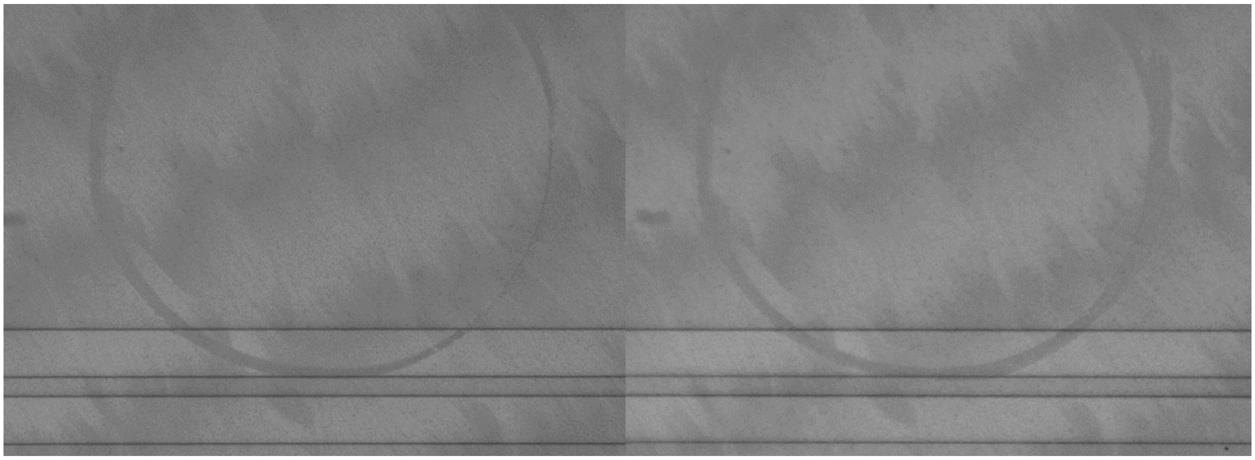

Figure 15: (left) The initial write of a disk resonator with a 14ns pulse, a 0.2 dB ND filter, a 0.02 mm/s travel speed, and a 2 kHz repetition rate. The material thicknesses here are given in the Sb_2S_3 design of Section 2.2. (right) The same ring after the bottom right quadrant was patched with a combination of selected toolpaths and manually dictated movement.

3.6 LASER WRITTEN DEVICES

As of this writing, I have not characterized any devices made on this platform. Despite writing ring resonators (*Figure 15*), straight waveguides (*Figure 16*), curved waveguides (*Figure 17*), and a grating coupler (Figure 18), characterizing these devices was difficult due to losses from the material and the grating couplers. While the propagation loss was minimized in Section 2.2, that design does not accommodate bent waveguides. To increase the mode confinement, the PCM layer must be thicker and/ or the Si_3N_4 layer must be thinner. Therefore, the straight waveguide shown in *Figure 16* is the only device I anticipate working with the design presented in Section 2.2. The thick 400 nm Si_3N_4 provides a a good coupling efficiency of about 20% in theory, but also reduces mode confinement. In experiment, each coupler introduced 15 dB of loss. Thus, an on-chip and an off-chip coupler introduce 30 dB of loss into a measurement. This is half of the noise floor of 60 dB in the measurement setup. 100 and 200 nm Si_3N_4 layers showed a simulated coupling efficiency of ~5% so their losses would likely preclude PIC measurement. 300 nm Si_3N_4 films had a theoretical coupling efficiency around 12%, so they seem a good compromise between coupling efficiency and mode confinement. When combined with a thick enough PCM layer, this higher mode confinement achieves bending radii under 100 µm. Insufficient mode confinement was likely the reason that the ring shown in *Figure 15* did not have a measurable resonance. The ring was purposefully over coupled to the etched waveguide, so light should have entered the ring, but when it did, it was likely unguided and absorbed by the Sb_2S_3.

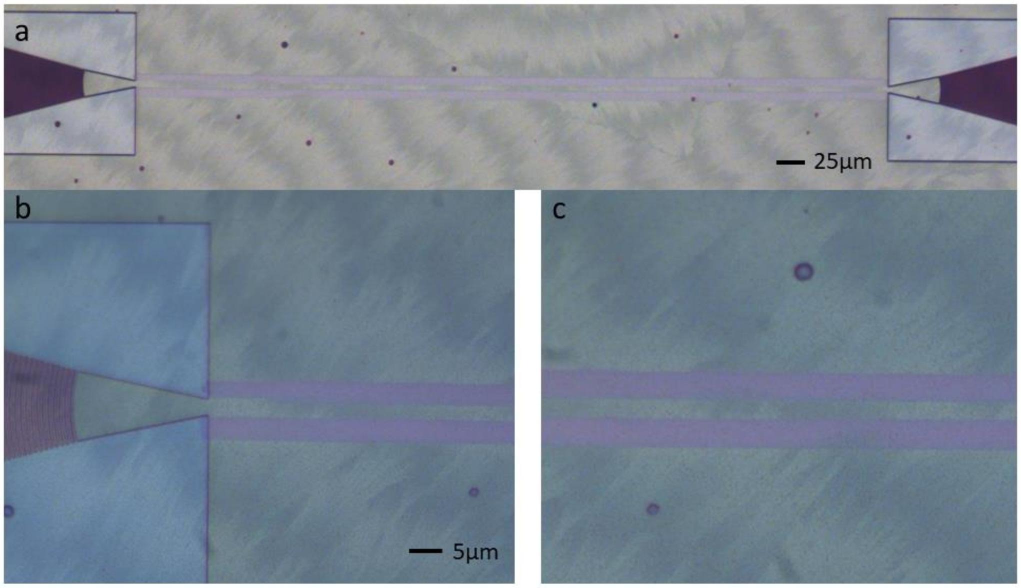

Figure 16: a) A 500 nm straight waveguide written between two grating couplers. The material and grating parameters here are given by the Sb_2S_3 design in Sections 2.2 and 2.3 b) A zoomed in image of the left coupler/ waveguide interface in image a. c) A zoomed in image of the center of the waveguide shown in image a.

Using a 300 nm Si_3N_4 layer, a 35 nm Sb_2S_3 layer, and revised grating coupler parameters, I drew bent waveguides to show guiding using a curved waveguide as shown in *Figure 17*.

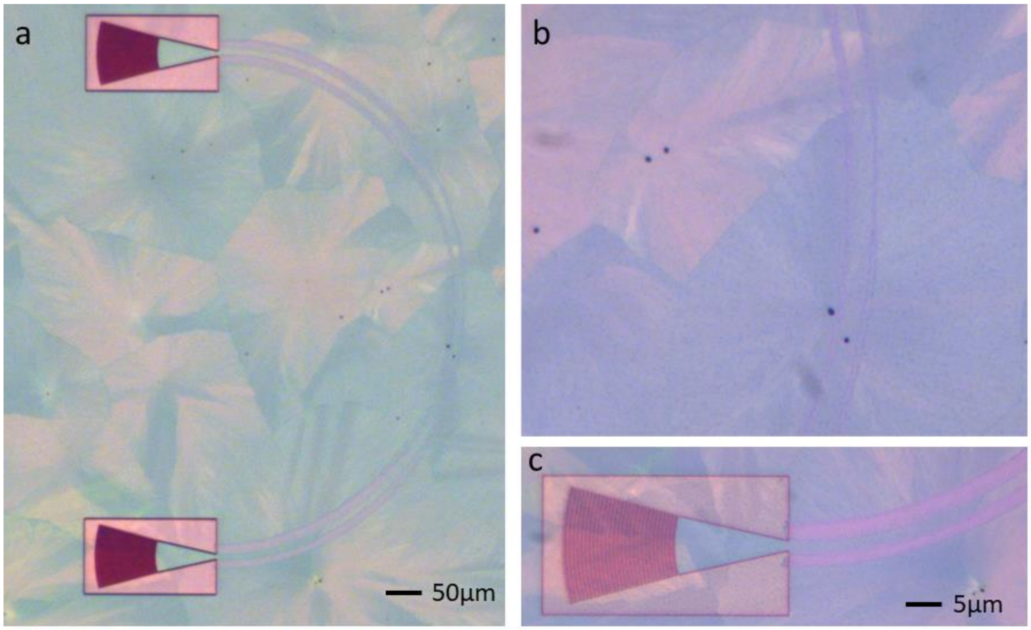

Figure 17: a) A circular waveguide with a 250 nm radius written on a 35 nm film of Sb_2S_3 *under a 300 nm layer of* Si_3N_4*. b) A zoomed in image of the rightmost region of the waveguide in a. The thinner walls are an example of improper focusing as a pattern is written. c) A zoomed in image of the lower grating/ waveguide interface in a.*

Either of these waveguide structures are straightforward to characterize but were not measured due to time constraints.

Chapter 4. CONCLUSION AND OUTLOOK

The field of integrated photonics would benefit greatly from an inexpensive and fast prototyping tool for PICs. While limited to passive PICs, this platform could allow sensitive parameters such as ring resonator coupling distance to be tested before the design is made in a nanofabrication facility. This work started by proposing a low-loss dielectric assisted waveguide structure that theoretically decreases propagation loss by a factor of 56 for Sb_2S_3 and 17 for Sb_2Se_3 over a traditional waveguide structure. The thermal dynamics of nanosecond heating pulses were also simulated, suggesting that nanosecond laser pulses can switch thin films of Sb_2S_3. These switching dynamics were confirmed by a purpose-built experimental setup.

While this setup drew various arbitrary patterns, their use as photonic devices remains to be realized. This is the key result that any future work should strive to observe. Additional endeavors include writing a dynamic focusing script that measures the contrast of the camera image and adjusts the focal plane and/ or incorporating lower NA objectives into the setup. The first would enable the stage's focus to account for variations on the chip that were observed during experiments. The source of these variations is unclear, but at some points, planar focusing was insufficient for maintaining focus throughout a write. Similarly, decreasing the NA of the objective lens would increase the depth of field, making focusing more forgiving. This would also decrease the resolution of the setup, so ideally the high NA objective would outline the pattern, but then a lower NA objective could fill in larger regions to be amorphized.

Currently this platform holds promise for inexpensively prototyping arbitrary PICs. If it is shown to make devices, then it will become a useful tool for PIC prototyping and photonic education.

[1] L. He, H. Li, and M. Li, "Optomechanical measurement of photon spin angular momentum and optical torque in integrated photonic devices," *Science Advances,* vol. 2, no. 9, p. e1600485, 2016, doi: doi:10.1126/sciadv.1600485.
[2] K. Wang *et al.*, "High-speed indoor optical wireless communication system employing a silicon integrated photonic circuit," *Opt. Lett.,* vol. 43, no. 13, pp. 3132-3135, 2018/07/01 2018, doi: 10.1364/OL.43.003132.
[3] J. Wang, F. Sciarrino, A. Laing, and M. G. Thompson, "Integrated photonic quantum technologies," *Nature Photonics,* vol. 14, no. 5, pp. 273-284, 2020/05/01 2020, doi: 10.1038/s41566-019-0532-1.
[4] S. Bandyopadhyay *et al.*, "Single chip photonic deep neural network with accelerated training," *arXiv,* 2022, doi: 10.48550/ARXIV.2208.01623.
[5] H. Zhou *et al.*, "Photonic matrix multiplication lights up photonic accelerator and beyond," *Light: Science & Applications,* vol. 11, no. 1, p. 30, 2022/02/03 2022, doi: 10.1038/s41377-022-00717-8.
[6] G. Rademacher *et al.*, "Peta-bit-per-second optical communications system using a standard cladding diameter 15-mode fiber," *Nature Communications,* vol. 12, no. 1, p. 4238, 2021/07/09 2021, doi: 10.1038/s41467-021-24409-w.
[7] J. A. Liddle, J. Bowser, B. R. Ilic, and V. Luciani, "So, You Want to Have a Nanofab? Shared-Use Nanofabrication and Characterization Facilities: Cost-of-Ownership, Toolset, Utilization, and Lessons Learned," (in eng), *J Res Natl Inst Stand Technol,* vol. 125, p. 125009, 2020, doi: 10.6028/jres.125.009.
[8] R. Chen, Z. Fang, F. Miller, H. Rarick, J. E. Fröch, and A. Majumdar, "Opportunities and Challenges for Large-Scale Phase-Change Material Integrated Electro-Photonics," *ACS Photonics,* vol. 9, no. 10, pp. 3181-3195, 2022/10/19 2022, doi: 10.1021/acsphotonics.2c00976.
[9] M. Wuttig and N. Yamada, "Phase-change materials for rewriteable data storage," *Nature Materials,* vol. 6, no. 11, pp. 824-832, 2007/11/01 2007, doi: 10.1038/nmat2009.
[10] R. Chen *et al.*, "Non-volatile electrically programmable integrated photonics with a 5-bit operation," *arXiv [physics.optics],* 2023 2023. [Online]. Available: http://arxiv.org/abs/2301.00468.
[11] M. Wuttig, H. Bhaskaran, and T. Taubner, "Phase-change materials for non-volatile photonic applications," *Nature Photonics,* vol. 11, no. 8, pp. 465-476, 2017/08/01 2017, doi: 10.1038/nphoton.2017.126.
[12] D. Loke *et al.*, "Breaking the Speed Limits of Phase-Change Memory," *Science,* vol. 336, no. 6088, pp. 1566-1569, 2012, doi: doi:10.1126/science.1221561.
[13] F. Miller, R. Chen, J. E. Froech, H. Rarick, S. Geiger, and A. Majumdar, "Rewritable photonic integrated circuits using dielectric-assisted phase-change material waveguides," *Opt. Lett.,* vol. 48, no. 9, pp. 2385--2388, May 2023, doi: 10.1364/OL.486403.
[14] J. Zheng *et al.*, "GST-on-silicon hybrid nanophotonic integrated circuits: a non-volatile quasi-continuously reprogrammable platform," *Opt. Mater. Express,* vol. 8, no. 6, pp. 1551-1561, 2018/06/01 2018, doi: 10.1364/OME.8.001551.
[15] M. Delaney, I. Zeimpekis, D. Lawson, D. W. Hewak, and O. L. Muskens, "A New Family of Ultralow Loss Reversible Phase-Change Materials for Photonic Integrated Circuits: Sb2S3 and Sb2Se3," (in English), *Adv Funct Mater,* vol. 30, no. 36, Sep 2020, doi: ARTN 2002447
10.1002/adfm.202002447.

[16] C. Ríos *et al.*, "Ultra-compact nonvolatile phase shifter based on electrically reprogrammable transparent phase change materials," *PhotoniX,* vol. 3, no. 1, p. 26, 2022/10/26 2022, doi: 10.1186/s43074-022-00070-4.

[17] Z. Fang *et al.*, "Ultra-low-energy programmable non-volatile silicon photonics based on phase-change materials with graphene heaters," *Nature Nanotechnology,* vol. 17, no. 8, pp. 842-848, 2022/08/01 2022, doi: 10.1038/s41565-022-01153-w.

[18] Z. Fang, J. Zheng, A. Saxena, J. Whitehead, Y. Chen, and A. Majumdar, "Non-Volatile Reconfigurable Integrated Photonics Enabled by Broadband Low-Loss Phase Change Material," *Advanced Optical Materials,* vol. 9, no. 9, 2021, doi: 10.1002/adom.202002049.

[19] K. Gao *et al.*, "Intermediate Phase-Change States with Improved Cycling Durability of Sb2S3 by Femtosecond Multi-Pulse Laser Irradiation," *Adv Funct Mater,* vol. 31, no. 35, 2021, doi: 10.1002/adfm.202103327.

[20] R. Chen, Z. Fang, J. E. Fröch, P. Xu, J. Zheng, and A. Majumdar, "Broadband Nonvolatile Electrically Controlled Programmable Units in Silicon Photonics," *ACS Photonics,* vol. 9, no. 6, pp. 2142-2150, 2022/06/15 2022, doi: 10.1021/acsphotonics.2c00452.

[21] F. Qiu *et al.*, "Ultra-thin silicon/electro-optic polymer hybrid waveguide modulators," *Applied Physics Letters,* vol. 107, no. 12, 2015, doi: 10.1063/1.4931490.

[22] J. Kischkat *et al.*, "Mid-infrared optical properties of thin films of aluminum oxide, titanium dioxide, silicon dioxide, aluminum nitride, and silicon nitride," *Appl. Opt.*, vol. 51, no. 28, pp. 6789-6798, 2012/10/01 2012, doi: 10.1364/AO.51.006789.

[23] G. De Paoli *et al.*, "Laser trimming of the operating wavelength of silicon nitride racetrack resonators," *Photon. Res.*, vol. 8, no. 5, pp. 677-683, 2020/05/01 2020, doi: 10.1364/PRJ.382529.

[24] Z. Fang, R. Chen, J. Zheng, and A. Majumdar, "Non-Volatile Reconfigurable Silicon Photonics Based on Phase-Change Materials," *IEEE Journal of Selected Topics in Quantum Electronics,* vol. 28, no. 3: Hybrid Integration for Silicon Photonics, pp. 1-17, 2022, doi: 10.1109/JSTQE.2021.3120713.

[25] F. Qiu *et al.*, "Athermal Hybrid Silicon/Polymer Ring Resonator Electro-optic Modulator," *ACS Photonics,* vol. 3, no. 5, pp. 780-783, 2016/05/18 2016, doi: 10.1021/acsphotonics.5b00695.

[26] J. R. Rumble, "CRC handbook of chemistry and physics," *CRC handbook of chemistry and physics*103 ed. Boca Raton, FL: CRC Press/Taylor & Francis, 2022.

[27] Q. Wang *et al.*, "Optically reconfigurable metasurfaces and photonic devices based on phase change materials," *Nature Photonics,* vol. 10, no. 1, pp. 60-65, 2016/01/01 2016, doi: 10.1038/nphoton.2015.247.

[28] K. Chaudhary *et al.*, "Polariton nanophotonics using phase-change materials," *Nature Communications,* vol. 10, no. 1, 2019, doi: 10.1038/s41467-019-12439-4.

Chapter 5. APPENDIX

5.1 ADDITIONAL RAMAN FIGURE

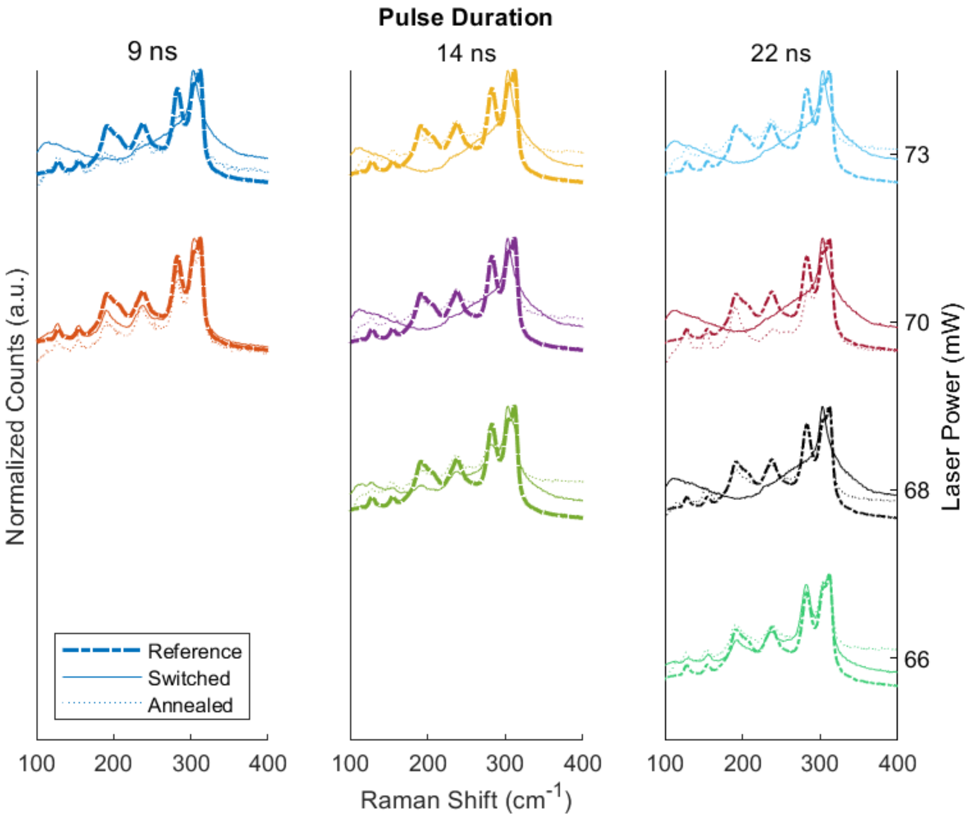

Figure 18: The full Raman spectra for the switching shown in *Figure 12*.